Carbon-induced strengthening of bcc iron at the atomic scale

Arnaud Allera,[1,2] Fabienne Ribeiro,[1] Michel Perez,[3] and David Rodney[2]
[1]*IRSN/PSN-RES/SEMIA/LSMA Centre d'études de Cadarache, 13115 Saint Paul-lez-Durance, France*
[2]*Université de Lyon, Université Claude Bernard Lyon 1, CNRS, Institut Lumière Matière, F-69622 VILLEURBANNE, France*
[3]*Université de Lyon, INSA Lyon, UCBL, MATEIS, UMR CNRS 5510 Villeurbanne, France*

(Received 8 September 2021; revised 7 December 2021; accepted 16 December 2021; published 18 January 2022)

In steels, the interaction between screw dislocations and carbon solutes has a great influence on the yield strength. Fe-C potentials used in molecular dynamics (MD) simulations yield a poor description of screw dislocation properties—their core structure and Peierls barrier—compared to *ab initio* calculations. Here we combine two EAM potentials from the literature, which greatly improves dislocation property accuracy in FeC alloys. Using this hybrid potential, MD simulations of dislocation glide in random solid solutions confirm a powerful solute strengthening, caused by complex interaction processes. We analyze these processes in a model geometry, where a row of carbon atoms is inserted in the dislocation core with varying separations. We use a combination of MD simulations, minimum-energy path calculations, and a statistical model based on the harmonic transition state theory to explain the strengthening induced by carbon. We unveil that carbon disrupts the glide process, as unpinning requires the successive nucleation of two kink pairs. When solute separation is below about 100 Burgers vectors, the activation enthalpy of both kink pairs are markedly increased compared to pure iron, resulting in a strong dependence of the unpinning stress on solute spacing. Our simulations also suggest an effect of carbon spacing on the kink-pair activation entropy. This work provides elementary processes and parameters that will be useful for larger-scale models and, in particular, kinetic Monte Carlo simulations.

DOI: 10.1103/PhysRevMaterials.6.013608

I. INTRODUCTION

The addition of carbon in iron to improve mechanical properties is at the basis of steel metallurgy [1]. However, the mechanism that controls the solute strengthening of the widely used body-centered-cubic (bcc) ferritic steels is not completely understood [2]. Low-temperature plasticity in these alloys is controlled by the mobility of screw dislocations [3,4], which is limited by both the strong resistance of the atomic lattice, and interactions with other defects [2], among which are interstitial carbon atoms. The lattice resistance is bcc metals is characterized by a large Peierls barrier that favors long straight segments along dense [111] directions [3]. For this reason, dislocation glide at low temperature consists in the thermally activated nucleation and subsequent propagation of kink pairs along the dislocation lines. The presence of interstitial carbon atoms affects this process, even with low concentrations of solutes [5]. Solute strengthening theories were proposed to model hardening in substitutional alloys [6–13] but their application to interstitial alloys — characterized by strong solute-dislocation interactions in the region of the core [14,15]— remains difficult.

Over the last decade, screw dislocation core properties have been studied using the density functional theory (DFT) [16], an *ab initio* method able to model atomic interactions at the electronic level. In iron and other pure metals, this approach was used to characterize the dislocation energetics [17–20] and its dependence on the applied stress [21,22]. In the Fe-C system, DFT calculations unveiled local effects of carbon, consisting in the stabilization of a prismatic core structure unstable in pure Fe [14]. This effect was also evidenced in other bcc metals [23] and with other interstitial solutes [15]. Due to its low mobility [24], this reconstructed prismatic core is expected to control the plasticity of bcc interstitial alloys when solutes are mobile and decorate the dislocations [25]. Though, the scale accessible to DFT lies under a thousand atoms in static simulations, which generally limits dislocation simulations to the Peierls mechanism, by which a straight dislocation moves from one stable position in the lattice to the next. Kink-pair formation and dynamical simulations remain so far accessible only to empirical potentials.

Classical molecular dynamics (MD) simulations in pure iron successfully reproduced the thermally activated kink pair mechanism [26,27]. MD simulations were also used to study the effect of carbon on nonscrew dislocations in iron [28–32], but simulating its effect on screw dislocations remains challenging. Screw dislocation locking by carbon was simulated using MD [33] and energetic computations [34–36], showing a dramatic reduction of dislocation mobility, linked to a higher kink-pair nucleation enthalpy [37]. However, the potentials used in these studies show a poor agreement with dislocation properties in iron computed with DFT -including the shape and height of the Peierls barrier- making their conclusions open to questions. The transferability issue is inherent to the use of semi-empirical potentials, which are greatly simplified models, often developed to address a specific question, with poor performance in systems far from their fitting domain

TABLE I. List of interatomic potentials and *ab initio* data used in this study.

Name	Type	Species	Ref.
Hepburn	EAM	Fe, C	[49]
Veiga	EAM	Fe, C	[50]
Becquart	EAM	Fe, C	[34]
Lee	MEAM	Fe, C	[51]
Henriksson	Tersoff	Fe, C	[52]
Liyanage	MEAM	Fe, C	[53]
DFT	*ab initio*	Fe, C	[19,34,54]
Ackland	EAM	Fe	[55]
Proville	EAM	Fe	[54]

[38]. The recent development of machine learning (ML)-based potentials for iron [39–41] opens exciting perspectives to improve the accuracy and transferability of interatomic potentials, but the computational cost of these models is 3 to 5 orders of magnitude larger than classical EAM [42]. Furthermore, no Fe-C ML potential is available to our knowledge, and recent attempts to develop efficient, classical potentials for Fe with the help of ML lead to poor screw dislocation properties [42,43].

In this paper, we compare several Fe-C potentials from the literature on a list of dislocation properties. As no potential was found fully satisfactory, a combination of two existing potentials is proposed. Using this potential (referred as "hybrid"), we simulated the glide of screw dislocations in random solid solutions of C atoms, showing the dominant role played by short-range core interactions compared to long-range elastic ones. The complexity of the processes seen in the random solid solutions led us to consider a simpler configuration, where a screw dislocation interacts with a row of C atoms of varying separation. We analyze in details this elementary process using a combination of MD simulations, saddle-point search methods, and a statistical model of the unpinning stress based on the harmonic transition state theory (HTST).

II. METHODS

A. Interatomic potentials

We tested several interatomic potentials for Fe-C alloys from the literature, presented in Table I. The potentials are based on different formalisms, namely, embedded atom method (EAM), modified embedded atom mMethod (MEAM), and Tersoff, all implemented in the LAMMPS MD package [44]. The Fe-C potentials from Becquart, Veiga, and Hepburn use the Fe interaction proposed by Ackland and therefore share the same properties in pure iron. While dislocation properties of the Ackland potential are known [45], the Fe part of Liyanage, Lee, and Henriksson potentials, which were respectively developed in Refs. [46–48] were never tested for dislocation properties. Table I also includes information about two EAM potentials for pure iron as well as *ab initio* DFT data, used for benchmarking. We focused on properties related to screw dislocation motion in Fe-C alloys, as a comprehensive assessment of Fe-C potentials is beyond the scope of this article.

For clarity, we refer to the interatomic potentials by the name of the first author of the associated publication, e.g., "Ackland potential."

B. Simulation setup

We consider screw dislocations with a $\vec{b} = \frac{1}{2}[111]$ Burgers vector, gliding in a $(\bar{1}10)$ plane and interacting with carbon atoms. In the rest of this paper, we note $b = \|\vec{b}\|$. To compare the predictions of interatomic potentials with *ab initio* data, we used a simulation setup typical of DFT calculations: a fully periodic simulation cell, containing a dipole of dislocations of opposite Burgers vectors [19]. With appropriately chosen repetition vectors [16,56], this setup allows to model a quadrupolar array of screw dislocations with alternating Burgers vectors, which minimizes the forces on the dislocations caused by their periodic images. The cell has a length $n \times b$ in the [111] direction, and the dimensions in $[\bar{1}\bar{1}2]$ and $[1\bar{1}0]$ directions are respectively set to $15 \times \sqrt{2/3}a_0$ and $9 \times \sqrt{2}/2a_0$, with $a_0 = 2.815$ Å, the bcc lattice parameter. It thus contains $n \times 135$ atoms, with n an integer.

For dynamical simulations, it is preferable to avoid fully periodic simulation cells, as the strong attraction between the dislocations of the dipole may result in cross-slip and dislocation annihilation. Instead, we used cells where we introduced a single screw dislocation along the $\vec{x} = [111]$ direction and applied periodic boundary conditions in the xy $(\bar{1}10)$ glide plane and free surfaces in the perpendicular $\vec{z} = [\bar{1}10]$ direction. These conditions generate a periodic array of dislocations (PAD) [2,57]. Different dimensions in the $\vec{x}$ direction L_x were tested, while dimensions along $\vec{y}$ and $\vec{z}$, referred to as L_y and L_z, were set to (138 Å, 159 Å) in dynamic simulations (192 000 atoms) and (138 Å, 80 Å) for static calculations (96 000 atoms). At finite temperature, a large z dimension is needed to lower the attraction of the free z surfaces on the dislocation, which tends to favor cross-slip.

Dynamical simulations were performed under constant strain rate, using the flexible boundary conditions presented in Ref. [58]. For this purpose, two slabs of atoms denoted S^+ and S^- are defined underneath the top and bottom z surfaces, with a thickness slightly larger than the interatomic potential cutoff radius (approximately 6 Å). An initial velocity is applied to all atoms of each slab, depending on the desired xz shear rate $\dot{\gamma}$:

$$v_{0,x}^{\pm} = \pm\dot{\gamma}\frac{L_z}{2}. \tag{1}$$

At every time step, the force in the $\vec{x} = [111]$ direction on each atom i in $S^{\pm}$ is corrected in order to ensure that the total force in S^+ and S^- is zero:

$$F_x^i \leftarrow F_x^i - \langle F_x \rangle^{\pm}, \tag{2}$$

where $\langle F_x \rangle^{\pm}$ refers to the average force in $S^{\pm}$ in the $\vec{x}$ direction. In this way, the centers of mass of the slabs move at a constant velocity, thus imposing a constant strain rate, while allowing atoms in $S^{\pm}$ to adapt to the motion of the dislocation [58]. All simulations were performed with an applied strain rate $\dot{\gamma} = 1 \times 10^7\ s^{-1}$.

All dynamical simulations were conducted in the NVE ensemble (i.e., without a thermostat). A temperature rise of a few kelvins is therefore observed due to the plastic work,

and is included in our reported data. Dynamical simulations were run using the GPU package of LAMMPS [59] to accelerate force evaluations. All visualizations were produced using the OVITO software [60].

C. Minimum energy paths

Identifying transition states between minimum energy states (MES) is key in approaches based on the HTST. Double-ended saddle-point search techniques, such as the nudged elastic band (NEB) method [61], are well suited for the study of systems in which the initial and final MES are easily determined, as is the case here. For this reason, we used the LAMMPS implementation of the NEB method to determine the Peierls barrier, i.e., the energy barrier between two consecutive straight screw dislocation configurations (Peierls valleys) in the $(\bar{1}01)$ glide plane. NEB calculations are conducted using a force criterion for convergence of 1×10^{-4} eVÅ^{-1}, a spring force set to 0.1 eVÅ^{-1}. The number of replicas is 48 for the evaluation of Peierls barriers.

However, this technique requires the use of a large number of replicas to converge to saddle states when the activation energy is small compared to the energy difference between initial and final states, i.e., when a large plastic work is generated between both states (see Sec. V). In that case, we used a quick NEB minimization with a loose force tolerance of 1×10^{-1} eVÅ^{-1} and eight replicas to estimate the saddle state, followed by an activation relaxation technique (ARTn) optimization [62,63], a single-ended saddle search method, with a stopping force criterion set to 2.5×10^{-5} eVÅ^{-1}.

III. ASSESSMENT OF INTERATOMIC POTENTIALS AND INTRODUCTION OF A NOVEL HYBRID POTENTIAL

For the simulation of screw dislocation motion in iron, key properties include the dislocation core structure and Peierls barrier. In Fe-C alloys, the carbon-dislocation binding energy is central for pinning and solute strengthening effects [7]. Additional alloy properties, namely the carbon-carbon binding energiy in bulk Fe and the elastic dipole tensor are presented in Ref. [64].

A. Dislocation core structure

In pure iron, it is well accepted that screw dislocations have a compact, nondegenerate easy core structure [16,65]. To test this property, we used a fully periodic simulation cell of thickness b in the $\vec{x}$ direction, in which a dislocation is inserted in an easy position, and a force minimization is performed with a convergence criterion of 1×10^{-6} eVÅ^{-1}. Almost all tested potentials predict a nondegenerate, easy compact core [shown in Fig. 1(a)], in agreement with *ab initio* results. But the potential of Lee predicts a degenerate core shown in Fig. 1(b), and Henriksson potential predicts a structure close to a hard core, both results being in disagreement with *ab initio* data and making these potentials unsuited for the simulation of screw dislocations.

In presence of an array of carbon atoms initially placed every $\vec{b}$ in the octahedral position nearest to the dislocation core (denoted $O^{(1)}$ in Ref. [14]), we observed for all tested potentials, a conversion from an *easy* to a distorted *hard* core

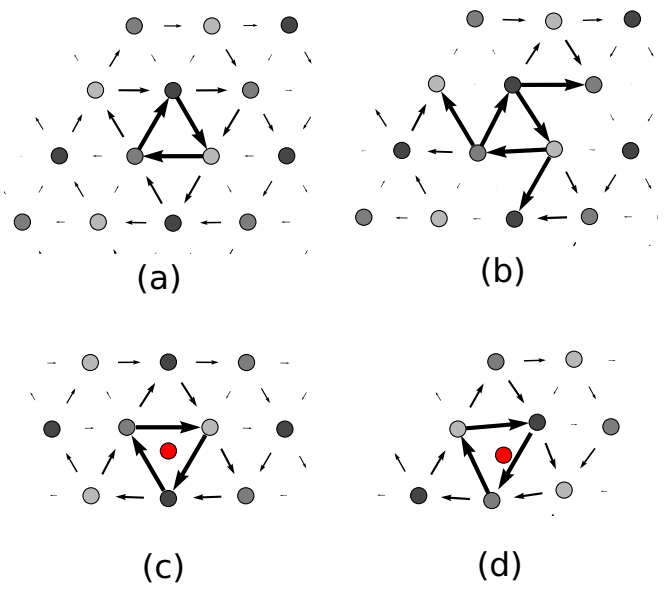

FIG. 1. Differential displacements of atoms in the dislocation core region. Different structures were obtained: (a) compact core (DFT, all potentials except Lee and Henriksson); (b) degenerate core (Lee); (c) symmetrical hard core (DFT); and (d) asymmetrical hard core obtained with the hybrid and other potentials (see text). Grey circles represent the relaxed position of Fe atoms. Red circles represent carbon atoms. Head-up triangles correspond to easy positions, while head-down triangles correspond to hard positions.

structure as the system was relaxed. The observed conversion is close to the behavior obtained with *ab initio* calculations, although the structures are slightly distorted and asymmetrical [see Fig. 1(d) for the structure obtained with the hybrid potential introduced at the end of this section], as opposed to the symmetrical structure found by DFT calculation [Fig. 1(c)].

B. Peierls barrier

Ab initio calculations determined that the Peierls barrier in pure Fe has a single maximum with a magnitude of 29 meV/b [19]. In Fig. 2, this result is compared to the Peierls barriers obtained with interatomic potentials predicting a stable easy core structure. It is well known that the EAM potential

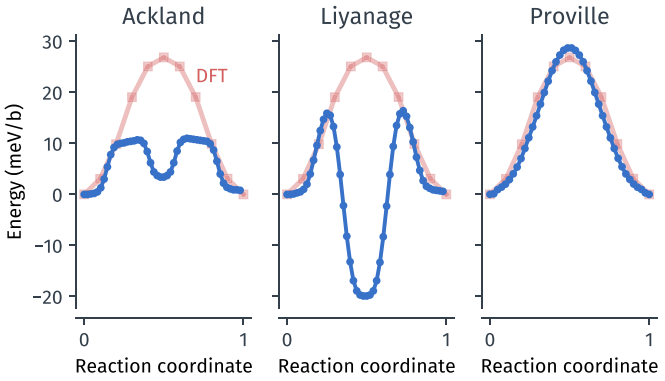

FIG. 2. Peierls barriers obtained with different interatomic potentials (blue dots) and compared to *ab initio* data [19] (red squares).

proposed by Ackland *et al.* [55] and used in the Fe-C Becquart potential for the Fe-Fe interactions predicts a metastable state in-between Peierls valleys [45,66]. This state corresponds to the *split* core, which is a local energy maximum according to *ab initio* results [18,20]. Similarly, Liyanage potential provides a poor description of the Peierls barrier, with an intermediate stable state with an energy lower than the easy core. Proville *et al.* developed a single-humped EAM potential [54], modified from Ref. [67], that quantitatively agrees with the *ab initio* Peierls barrier, as seen in Fig. 2. We note that the kink pair nucleation energy predicted by this potential is ∼0.6 eV [11]. This value is lower than estimations based on DFT-parameterized line tension models that are in the range 0.73-0.91 eV [18,21,68] or based on experimental data, 0.83 eV [69]. Despite this discrepancy, Proville potential remains the best candidate to simulate dislocation glide in bcc iron with a low computational load, and was adopted by other authors [11,70,71]. Recent ML-based potentials from Ref. [72] yield more realistic values (0.77 and 0.84 eV) and are promising for future work but will require an extension to include Fe-C interactions.

C. Carbon-dislocation binding energy

The binding energy of carbon atoms to dislocations is of great importance in the mechanism of solute strengthening [7] and is close to −0.7 eV in the Fe-C system—denoting an highly attractive interaction—according to *ab initio* results [24]. It was calculated as the energy difference per Burgers vector between a dislocation decorated by carbon atoms ($E_{d+\mathrm{C}}$), evenly spaced at a distance d_{CC} along the dislocation, and a dislocation in pure iron (E_d), minus the energy associated with the introduction of a carbon atom in bulk iron ($E_{b+\mathrm{C}} - E_b$) [15]:

$$E_{\mathrm{binding}}(d_{\mathrm{CC}}) = \tfrac{1}{2}[E_{d+\mathrm{C}}(d_{\mathrm{CC}}) - E_d] - [E_{b+\mathrm{C}} - E_b]. \quad (3)$$

Here, $E_{b+\mathrm{C}}$ is the energy per b of a cell that contains one carbon atom in an octahedral position, and E_b is the energy of the same cell with no solute atom. The factor $1/2$ accounts for the fact that there are two dislocations in the cell.

As seen in Fig. 3, the binding energy is negative, for all potentials except Hepburn, meaning an attraction of the carbon atoms to the dislocations. Among the potentials predicting an attraction, the magnitude of the energy varies widely, with more than a twofold underestimation in the case of Becquart and Veiga potentials, and almost a twofold overestimation in the case of Liyanage. Henriksson, Lee, and the Hybrid potential show a good quantitative agreement with *ab initio* results [24].

D. Construction of an hybrid interatomic potential

Here, we showed that Proville potential features a Peierls barrier in good agreement with DFT data (see Fig. 2), along with the correct dislocation core structure, but this potential is limited to pure iron. Fe-C potentials that predict the most accurate carbon-dislocation binding energy (Henriksson and Lee) do not predict the correct core structure in iron and should be avoided for simulations of screw dislocations.

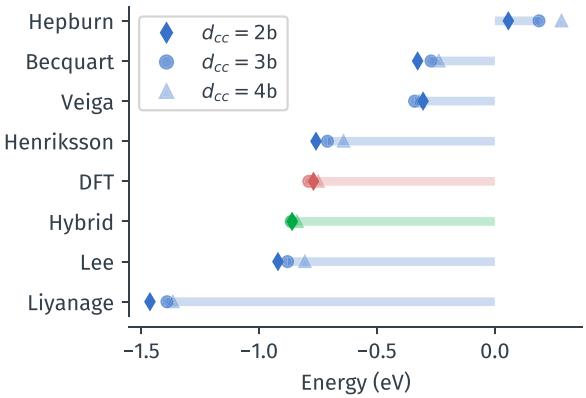

FIG. 3. Carbon-dislocation binding energy obtained with different interatomic potentials and for different carbon spacings d_{CC} (represented by different symbols) and compared to DFT data [24]. Horizontal lines serve as guides for the eye.

Veiga potential, a version of the Becquart potential corrected to improve interstitial sites stability [50], qualitatively agrees with DFT on carbon-carbon and carbon-dislocation binding energies even though its Fe properties are not satisfying. It was used in previous studies to investigate carbon-dislocation interactions, Cottrell atmosphere formation, and locking mechanisms [30,33,73]. Both Proville and Veiga potentials are EAM potentials derived from the seminal Mendelev potential [67]. We thus propose here an hybridization of both potentials to combine their advantages, while ensuring that the original Fe properties of Proville potential are preserved. This is enabled by a simple rescaling of the electronic density function, in a way that optimizes the C-dislocation binding energy compared to DFT data, with the result presented in Fig. 3 (see Ref. [64] for more details). All pure Fe properties of the hybrid potential are therefore the same as the original Proville potential. The Hybrid potential will be used in the rest of this paper and is made available for the community [64]. In additional tests, we obtained a migration barrier for C interstitials of 0.96 eV, which is close to the *ab initio* value of 0.90 eV [34], but with a rough energy landscape around the migration path between octahedral sites. We thus do not recommend this potential for studies on diffusion mechanisms, or with large C concentrations where solutes occupy adjacent lattice sites.

IV. DISLOCATION MOBILITY IN A SOLID SOLUTION

We start by simulating the glide of a screw dislocation interacting with a random solid solution of C atoms. In order to observe several pinning-unpinning events in the course of a MD simulation, and the combined effect of several C atoms along the dislocation, we set the concentration to 0.52 at%, i.e., 1000 solute atoms in a box containing 192 000 Fe atoms. The latter was created by inserting carbon atoms in octahedral sites randomly selected in the PAD simulation cell. Considering the short simulated time (a few nanoseconds) and the investigated temperatures, carbon atoms are not able to diffuse and are considered immobile in the rest of this paper.

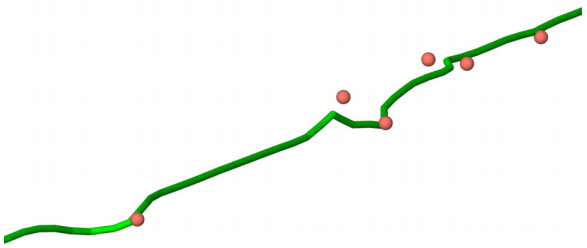

FIG. 4. Dislocation line (green) adopting a complex three-dimensional kinked structure in presence of carbon atoms (red spheres). Only the solutes closest to the dislocation are represented for clarity. The dislocation line was identified using the DXA algorithm [74].

Using the DXA algorithm [74], we can visualize the position of the dislocation line in MD simulations. Due to the high carbon-dislocation binding energy, nucleation of kink pairs in directions where carbon atoms are present is favored, which includes cross-slip planes. This results in strongly locked configurations, as illustrated in Fig. 4, where the dislocation line connects all neighboring C atoms, with segments extended in different planes giving the dislocation a three-dimensional shape.

Typical stress-strain curves are shown in Fig. 5(a). As shear is increased at a constant rate, the internal stress raises linearly before the flow stress is reached or each time the dislocation is in a pinned configuration. After each unpinning event, the stress drops as the dislocation rapidly glides in the cell to the next obstacle, resulting in a strongly serrated stress-strain curve. Unpinning stresses are on the order of 600 MPa at 300 K, compared to a flow stress of about 350 MPa in pure

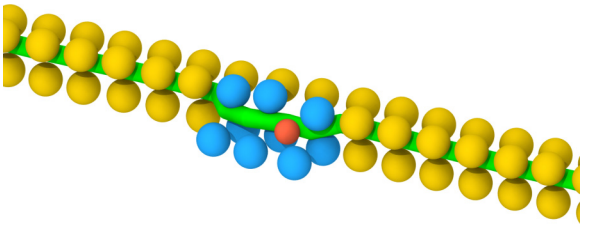

FIG. 6. Local conversion of the screw dislocation core during a dynamical simulation. The smaller red atom is a carbon atom, while all others are iron atoms. Iron atoms that adopt a distorted prismatic structure near the carbon atom, are highlighted in blue. The dislocation line obtained using the DXA algorithm is shown in green. For clarity, only core atoms are shown.

Fe [the stress-strain curve in pure Fe is shown in gray in Fig. 5(a)]. Strengthening can emerge from three mechanisms in the region of the core [7]: (i) solutes block the kink migration along the line, (ii) the interaction between kinks in different planes result in cross-kink pinning, and (iii) the nucleation of kink pairs on segments between solutes can becomes harder, especially with a reconstructed dislocation core (see Sec. V C). The local conversion of the dislocation core to a prismatic structure in the neighborhood of carbon atoms is indeed observed in dynamic simulations, as illustrated in Fig. 6.

As the interplay between the different strengthening mechanisms makes solid solution simulations too complex to analyze, simplifications are needed. In order to confirm the importance of short-range solute-dislocation interactions, we artificially created a carbon-free volume around the glide plane as illustrated in Fig. 5(b). Solute atoms outside this volume are left unchanged between the different simulations. In Fig. 5(a), we compare the stress-strain curves obtained with a full solid solution ($n_{\text{planes}} = 0$), and a carbon-depleted zone around the dislocation glide plane comprised of n_{planes} atomic

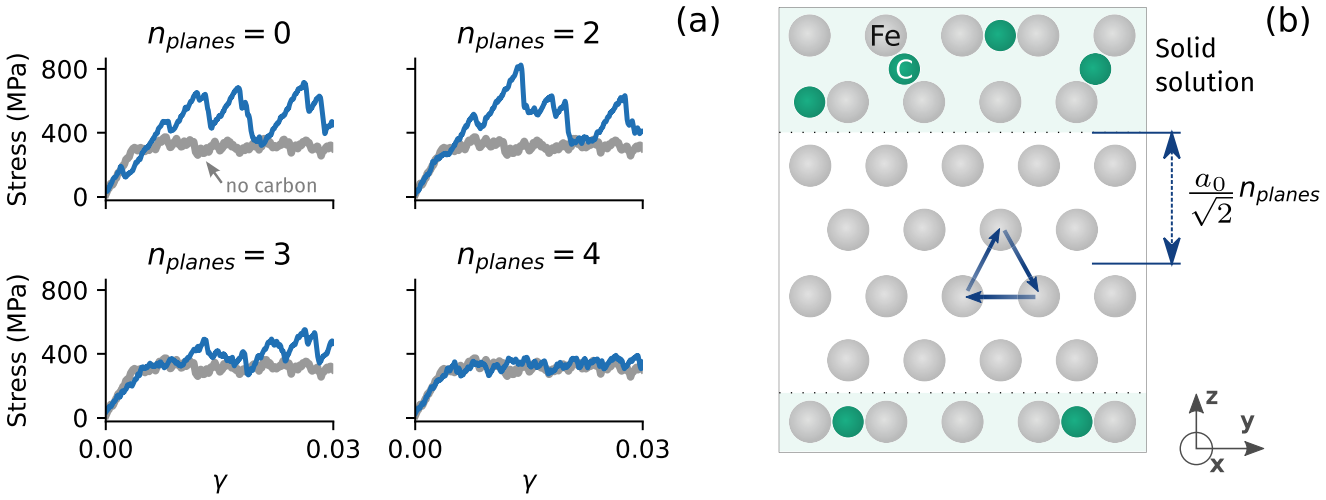

FIG. 5. Constant shear rate simulations with a carbon-depleted zone around the glide plane. (a) Stress-strain curves obtained at 300 K. Blue lines represent simulations in which a carbon depleted zone of n_{planes} atomic planes above and below the glide plane was created, as illustrated in (b). The case $n_{\text{planes}} = 0$ corresponds to a full random solid solution with a carbon concentration equal to 0.52 at%. In the case $n_{\text{planes}} = 2$, the dislocation cross slips to the solid solution due to the attraction of solutes, resulting in a stress curve that is similar to the full solid solution case. The gray line in (a) represents the same deformation test conducted in pure Fe.

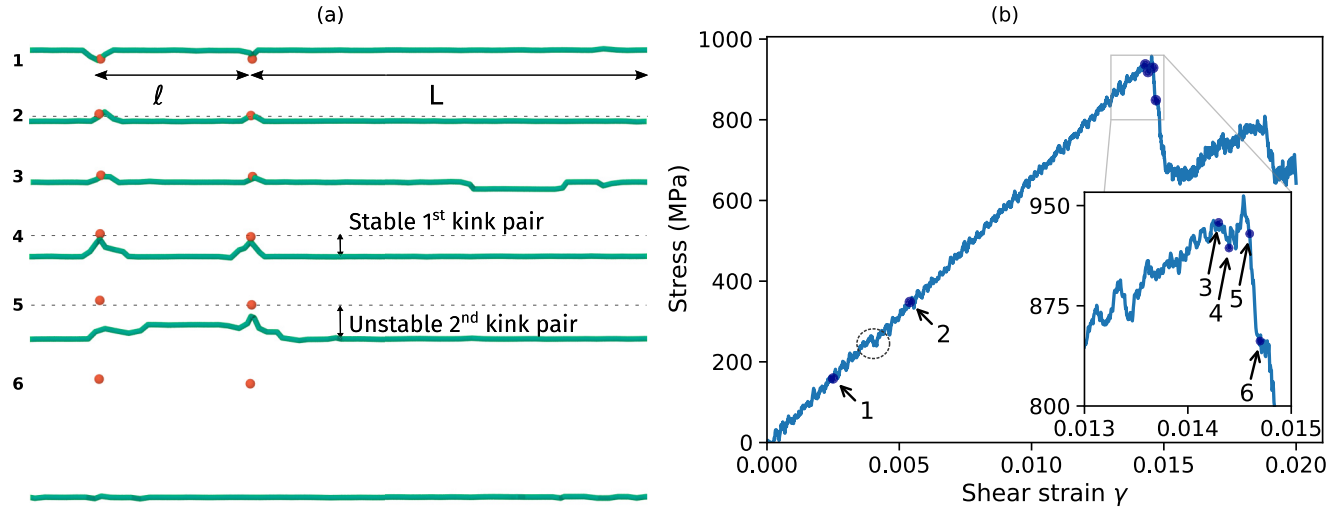

FIG. 7. Unpinning process for a dislocation pinned by two carbon atoms. (a) Snapshots taken at typical stages. The dislocation line as identified by the DXA algorithm is in green, carbon atoms are red spheres. Dashed lines serve as a visual guide. Between steps 3 and 4, a kink pair nucleates on the long segment, expands until being blocked by the carbon solutes, and spontaneously induces nucleation on the short segment. (b) Corresponding stress-strain curve. Numbers in (b) refer to the images in (a). Carbon atoms are separated by $\ell = 10b$ along a $40b$ dislocation. The MD simulation was conducted at 40 K for 2 ns with a strain rate of $1 \times 10^7\ \mathrm{s}^{-1}$.

planes on both sides. It can be seen that the stress-strain curve obtained for $n_{\mathrm{planes}} = 2$ shows a similar strengthening than the case $n_{\mathrm{planes}} = 0$. This is caused by cross-slip of the dislocation, which is strongly attracted to C atoms —and to a lesser extend, to the free surfaces on top and bottom of the simulation cell. Once the dislocation has cross-slipped (in an early stage of the simulation), it reaches a C-rich region, causing a strengthening similar to the case $n_{\mathrm{planes}} = 0$. On the other hand, cross slip does not happen for $n_{\mathrm{planes}} > 2$, where the dislocation remains in its initial (110) plane in the C-depleted zone. When n_{planes} is larger than 4, the stress level reveals no significant strengthening in comparison to pure iron (gray curve). Our conclusion is therefore twofold: (i) at moderate temperature (300 K), the capture radius of C atoms around the dislocation is $\sim\sqrt{2}a_0$. Within this distance, pinning is caused by the interaction of C atoms with the dislocation core, which is treated in the rest of this paper. (ii) Above this distance, elastic C-dislocation interactions have a comparatively limited effect, and vanish for a distance of $\sim 2\sqrt{2}a_0 \sim 8$ Å. In the next section, we thus neglect mid- and long-range C-dislocation interactions, and focus on the pinning/unpinning mechanisms in the dislocation core region.

V. UNPINNING FROM AN ARRAY OF C ATOMS

Given the complexity of dislocation glide in a random solid solution seen in previous section, we will consider a model system where a screw dislocation detaches from an array of carbon atoms directly located in its core. This allows to exclude cross-kink pinning, and the effect of mid- and long-range interactions, to focus on the elementary unpinning process. For these simulations, two C atoms were inserted in second-nearest octahedral positions along the dislocation line (denoted $O^{(2)}$ in Ref. [14]), aligned in the [111] direction inside the dislocation glide plane to avoid cross-slip. Due to the periodic boundary conditions in the [111] direction, the carbon atoms form an infinite one-dimensional array with a spacing between carbon atoms defined by two lengths: ℓ and L, with $\ell \leqslant L$ as illustrated in Fig. 7(a).

A. Unpinning mechanism at finite temperature

Figure 7 details the full unpinning processes of a dislocation, with the corresponding stress-strain curve, simulated with $\ell = 10\,b$ and $L = 30\,b$. A low temperature of 40 K was used to reduce thermal fluctuations, allowing to visualize the different stages more clearly. A step-by-step visualization of the MD simulation can be decomposed in six successive images shown in Fig. 7(a). The position of the dislocation core is identified using the DXA algorithm [74]. A caveat of this method is that kinks appear sharp, while they are of mixed character, with a width close to $w = 10\,b$ according to Ref. [11] who used the disregistry method [19] to localize the position of the core. The dislocation is initially in the Peierls valley before the C atoms (step 1). It jumps to the valley just after the C atoms (step 2) at a relatively low stress of about 250 MPa, which is marked by a slight stress drop highlighted by a dashed circle in Fig. 7(b). The magnitude of the stress drop is $\Delta\tau = \mu\rho bd$ (d is the distance between Peierls valleys) and corresponds to the plastic work associated with the jump. This configuration is the true pinning configuration, which resists dislocation motion until a high applied stress of about 950 MPa. At this point, a bulge forms on the longer L segment (step 3), where a kink pair nucleates. The kink pair then expands until it reaches the C atoms. The kinks are stopped at the C atoms that act as strong obstacles. In the simulations, we observed that the nucleation of this first kink-pair on the longer segment systematically triggered the nucleation of a second kink pair on the shorter segment. This can be explained by the strong elastic attraction between both screw segments, which adds up to the applied stress to help kink pair nucleation. As a result, the

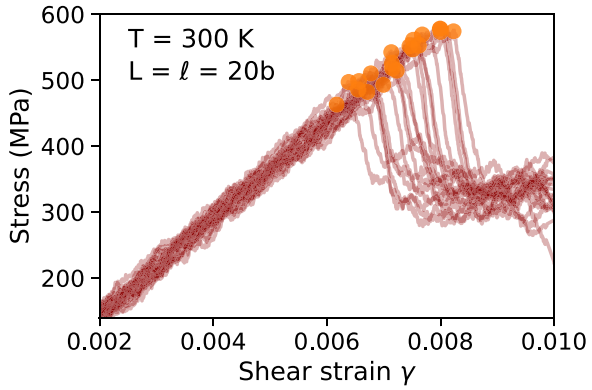

FIG. 8. Effect of the random initial velocity on the unpinning stress. Stress-strain curves obtained with C atoms every 20 b along the dislocation segment, at 300 K. Twenty different random seeds are used for the initial atomic velocities. The unpinning stress τ^* is marked by orange circles.

configuration where one segment has jumped while the other has not appears unstable in these conditions, and rapidly transits to the configuration shown in step 4, where each C atom is surrounded by two kinks of opposite sign. Step 4 is followed by a short period of stress increase, which suggests that this atomic configuration is stable under the applied stress, i.e., two kinks on both sides of the C atoms cannot annihilate, at least on short timescales. Between steps 4 and 5, a second kink pair nucleates on the longer segment, which causes unpinning followed by a large stress drop on the stress-strain curve in Fig. 7(b).

C atoms are therefore obstacles strong enough to block the annihilation of kinks despite the strong attractive kink-kink elastic interactions, and the large potential energy gain associated with kink annihilation. Under a typical applied stress of 600 MPa, the annihilation energy can be estimated as the kink-pair formation energy (0.6 eV) plus the work of the applied stress over the area swept by the annihilating kinks, $\sim\tau bdw \sim 0.6$ eV (with $w \sim 10\,b$ the kink width). The annihilation energy is thus >1 eV, larger than the C-dislocation binding energy (∼0.85 eV). Moreover, unpinning by a single kink-pair would leave a C atom in a first-neighbor position to the dislocation, which is an unstable configuration due to the finite capture radius of a dislocation to a C atom. The nucleation of a second kink pair is therefore needed, which creates a kink with a height of two Peierls valleys. This extended kink is able to cross the C atom [left C atom in step 5 of Fig. 7(a)], leading to the unpinning of the entire dislocation.

Nucleation of kink pairs is a thermally activated process, such that the unpinning stress τ^* is a random variable affected by the random seed of the initial atomic velocities. This effect is illustrated in Fig. 8. To account for this, we performed n repetitions for each MD simulation with different random seeds, and computed the average unpinning stress $\langle\tau^*\rangle$. The uncertainty $\sigma/\sqrt{n}$ is represented as error bars in the rest of this paper, where σ is the standard deviation of a series of n independent measurements of τ^*. In order to minimize $\sigma/\sqrt{n}$, we used values of n ranging from 5 to 20.

B. Effect of solutes spacing

We investigated the effect of solute spacing by varying ℓ and L on dislocations of varying $\ell + L$ total lengths. However, we observed that the length of the shorter ℓ segment has a negligible effect, such that all results can be presented in Fig. 9 as a function of L only. The figure also contains the flow stress computed in pure iron, which does not show any significant dependence on the dislocation length.

By way of contrast, the average unpinning stress in presence of C atoms shows a very strong L dependence when $L \lessapprox 100\,b$. $\langle\tau^*\rangle$ reaches more than 1 GPa when solutes are closest, meaning that the stress required to overcome them is more than twice the flow stress and is actually even higher than the 0 K Peierls stress in pure Fe (∼1 GPa). This demonstrates the powerful locking capability of an array of C atoms, with a spacing in the range 5 to ∼50 b when the temperature is small enough that the solute atoms cannot follow the dislocation in its glide. This very strong pinning for closely spaced C atoms is consistent with DFT calculations [15]. For larger C spacings, the unpinning stress reduces to the flow stress in pure iron and no strengthening or weakening is observed when $L \gtrapprox 100\,b$.

In addition, as mentioned above, the data show only a small difference in $\langle\tau^*\rangle$ whether the dislocation is pinned by evenly ($\ell = L$, red squares) or unevenly spaced C atoms ($\ell \leqslant L$, blue circles). The latter case was investigated by repeated simulations with different values of ℓ, ranging between 0 and L, which is why different data points share the same L in Fig. 9.

C. Effect of C atoms on kink pair nucleation enthalpy

1. NEB calculations

In order to better understand the origin of the very strong pinning induced by the C atoms at short distance, we used the NEB method to identify the minimum energy paths that connect the different stages of unpinning identified in MD simulations [i.e., stages presented in Fig. 7(a)], followed with an ART convergence to identify precisely the saddle configurations. We consider here the case $L = \ell$ where only one C atom needs to be inserted in the simulation cell. The reference state for the NEB calculations, S_0, is constructed in the same way as in the dynamic simulations, by inserting a C atom in an $O^{(2)}$ site, and relaxing the system. Final states are constructed by introducing the dislocation in different Peierls valleys in the glide direction. The initial NEB path was obtained by linear interpolation between the initial and final states.

Equilibrium and activated states for a dislocation with $L = 30\,b$ at an applied stress of 600 MPa are shown in Fig. 10(a), with the corresponding energy barriers in Fig. 10(b). Note that the enthalpy globally decreases due to the work of the applied stress, which tilts the potential energy landscape.

The unpinning process involves the successive nucleation of two kink pairs, between S_1 and S_2 and between S_2 and S_3. As can be seen in Fig. 10(a), the kink pairs in the activated states ($S_1^\star$ and $S_2^\star$) have not formed at the C atom, but rather in-between the C atom and one of its periodic images. The configuration S_2 contains two kinks on either side of the C atom. It is metastable. This confirms the MD observation that kinks of opposite signs cannot spontaneously annihilate

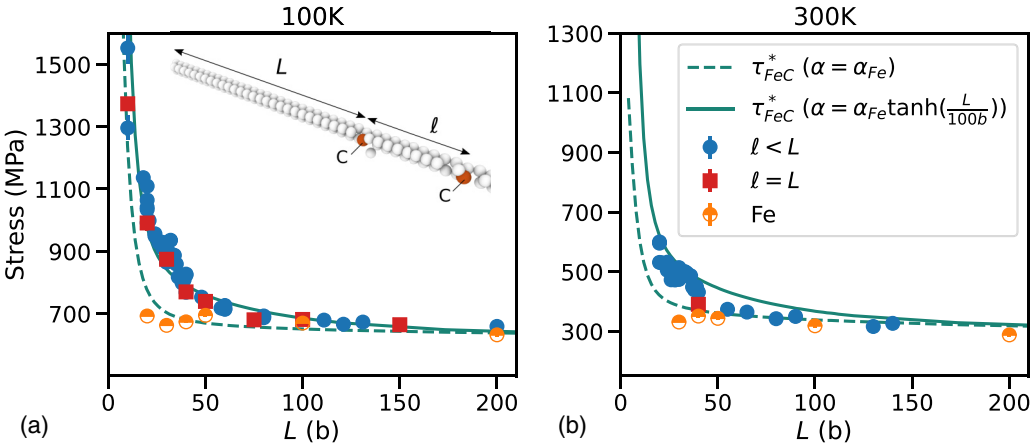

FIG. 9. Dependence of the average unpinning stress on the largest dislocation segment length L, computed during MD simulations at (a) 100 and (b) 300 K. Blue circles are when $\ell < L$, red squares when $\ell = L$. Half-filled orange symbols refer to the flow stress in pure iron computed by MD in cells of different lengths L. The dashed and solid lines are predictions of a statistical model (see text for details).

across C atom. The enthalpy barrier to form this first kink pair is noted ΔH_1. A second barrier of height ΔH_2 has to be overcome to form a second kink pair (state $S_2^\star$) and release the dislocation. This also confirms the MD observation that a kink crossing two Peierls valleys can overcome a C atom and unpin the dislocation. The next valleys (not shown here) are crossed with activation barriers close to that in pure Fe, ΔH_{Fe}. During unpinning, the C atom transits from the reconstructed core structure (in S_1, where it is in the dislocation core) to an octahedral position after the dislocation is released (in S_3). It can be noted that the activated states S_1^* and S_2^* are associated with small displacements of the carbon atom compared to the respective initial configurations, S_1 and S_2, as the transition is triggered by kink nucleation away from the C atom. Migration of the C atom from a prismatic to an octahedral position is therefore a consequence and not a limiting process for unpinning.

Figures 10(c) and 10(d) show examples of activation barriers for dislocation lengths $L = 20$ and $60\,b$ as well as in pure Fe. When L is small (20 b), we observe a significant

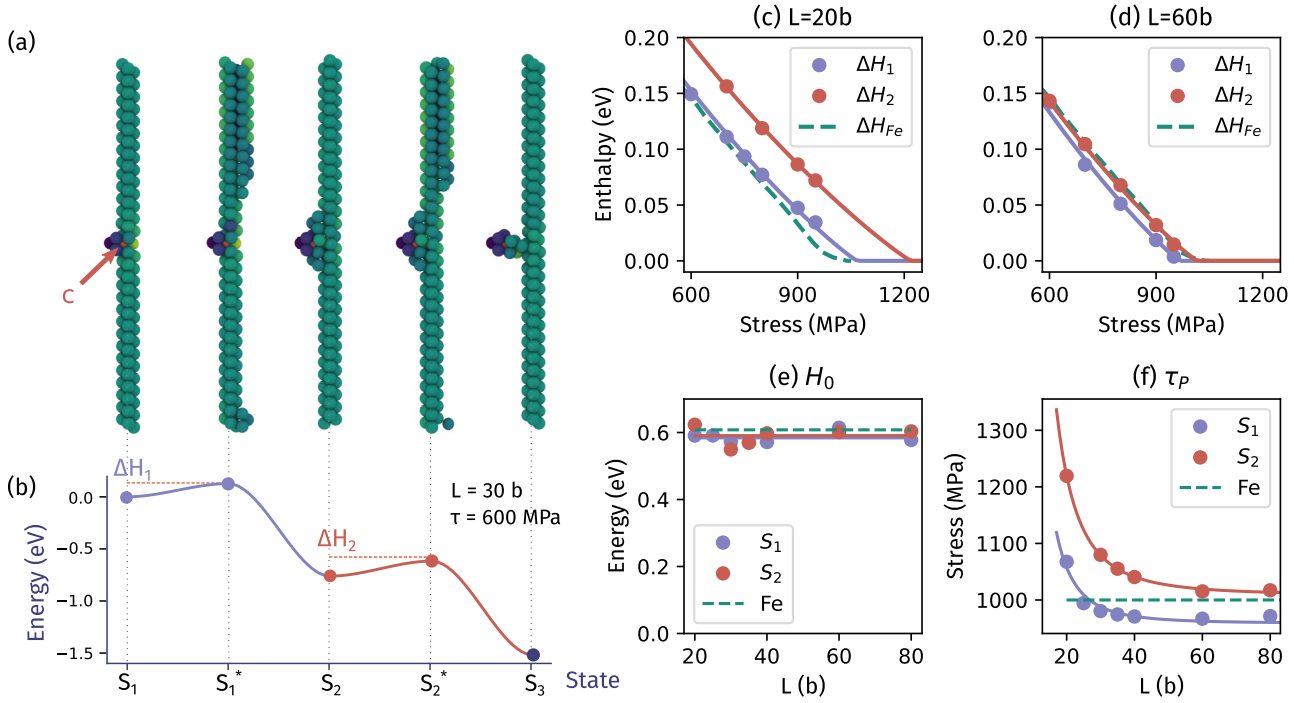

FIG. 10. NEB calculations of the two-step unpinning process of a dislocation from a row of C atoms. (a) Successive metastable and activated states during the unpinning process for a segment length of 30b and an applied stress of 600 MPa. Core atoms were identified using the centrosymmetry parameter [75]. (b) Corresponding energy profile. (c) and (d) show the activation enthalpies of both transitions ΔH_1 and ΔH_2 (circles) for two different solute separations. The solid lines are fits using Kocks' law [Eq. (9)]. (e) and (f) show the fitted parameters $\Delta H_{0,i}$ and $\tau_{P,i}$ of Kocks' law. Solid lines in (e) and (f) represent the average of ΔH_0 and a fit of τ_P using Eq. (10) for both transitions. Dashed lines in (c) to (f) represent the corresponding quantities in pure iron.

increase of ΔH_2 compared to ΔH_1, which remains close to ΔH_{Fe}. Therefore the C atom does not affect significantly the nucleation of the first kink pair, but the presence of this kink pair which cannot annihilate because of the C atom makes nucleation of the second kink pair much harder. This increase is at the origin of the strengthening seen in the MD simulations. Conversely, larger values of L (60 b) yield almost no change compared to pure iron. When the C atoms are widely separated, the kink pairs, which form away from the C atoms, no longer feel the presence of the solute atoms. We note a slight decrease of ΔH_1, implying that the C atoms help somewhat the nucleation of the first kink pair. However, since ΔH_2, which controls the unpinning, matches ΔH_{Fe}, no softening is produced, as confirmed by the MD simulations.

2. Statistical model

In order to connect the energy barriers with the MD simulations, we used a statistical model based on the HTST to predict the average unpinning stress. This model is adapted from Ref. [58], which considered thermally activated glide in absence of obstacles.

The central quantity of the statistical model is the survival probability, $W(t,t')$, the probability that the system in a metastable state at time t remains in that state until t', written

$$W_i(t,t') = \exp\left(-\int_t^{t'} p_i(\dot{\tau}_0 u)\,du\right). \tag{4}$$

It is a function of the transition rates, i.e., the probabilities per unit time, $p_{i=1,2}(\tau, L, T)$, that the dislocation jumps from S_1 to S_2 ($i=1$) and from S_2 to S_3 ($i=2$). These rates are functions of the dislocation length L and the temperature T as well as the applied stress τ. Since the MD simulations are strain-rate controlled, the stress increases linearly with time, at a rate $\dot{\tau}_0 = \mu\dot{\gamma}$, where μ is the shear modulus. The probability $W(t)$ that, starting at $t=0$ in an unstrained system, the dislocation is still pinned at time t, is related to W_1 and W_2 as

$$W(t) = W_1(0,t) - \int_0^t \frac{\partial W_1}{\partial t'}(0,t^\star) W_2(t^\star, t)\,dt^\star, \tag{5}$$

where the first term is the probability that the dislocation is still in state S_1 at time t and the second term is the probability that the dislocation jumps from S_1 to S_2 at time $t^\star \in [0,t[$ but then remains in S_2 until t.

Substituting the expression of W_i, we obtain

$$\begin{aligned} W(t) = {} & \exp\left(-\int_0^t p_1(\dot{\tau}_0 u)\,du\right) \\ & + \int_0^t \left[p_1(\dot{\tau}_0 t^*)\exp\left(-\int_0^{t^*} p_1(\dot{\tau}_0 u)\,du\right)\right. \\ & \left. \times \exp\left(-\int_{t^*}^t p_2(\dot{\tau}_0 u - \Delta\tau)\,du\right)\right] dt^*. \end{aligned} \tag{6}$$

The probability to unpin at time t is given by $\omega(t) = -dW/dt$ and the average unpinning stress is thus

$$\langle \tau^\star \rangle = \mu\dot{\gamma}\int_0^\infty t\,\omega(t)\,dt \tag{7}$$

To compute $\langle \tau^\star \rangle$, we thus need to express the rates, $p_{i=1,2}(\tau, L, T)$. Within the HTST [58], they are written as

$$p_i(\tau, L, T) = \nu\frac{L}{b}\exp\left(\frac{-\Delta G_i(\tau, L, T)}{kT}\right), \tag{8}$$

where ν is an attempt frequency and ΔG is the Gibbs activation energy of the process. $\Delta G = \Delta H - T\Delta S$ is notoriously difficult to compute [76] and approximations are often used. The first is to consider the harmonic regime, where ΔH and ΔS do not depend on T and $\Delta H(\tau, L)$ is directly obtained from the zero Kelvin MEP computed in previous section. Another classical approximation is to assume that ΔS is a constant, which can then be incorporated in the attempt frequency ν, such that the transition rates depend only on ΔH. This approximation has been shown valid in the case of a Lomer dislocation in aluminum in Ref. [58]. However, ongoing calculations using the projected average force integrator (PAFI) method [76] show a linear stress dependence of ΔS that cannot be neglected in the case of screw dislocation glide in bcc metals. The description of these calculations is beyond the scope of the present paper, which is focused on the effect of carbon. They will be presented in a forth-coming publication [77]. Here, we will use as a first approximation the parameters determined in pure iron with Proville potential: $\nu = 5\times10^{10}\,\mathrm{s}^{-1}$ and $\Delta S = k_B\alpha_{\mathrm{Fe}}\tau$ with $\alpha_{\mathrm{Fe}} = 1.28\times10^{-2}\,\mathrm{M\,Pa}^{-1}$.

Finally, computing Eq. (8) requires a continuous expression of $\Delta H_i(\tau, L)$. For this purpose, we used a classical Kocks law [66]:

$$\Delta H_i(\tau, L) = \Delta H_{0,i}(L)\left(1 - \left(\frac{\tau}{\tau_{P,i}(L)}\right)^p\right)^q. \tag{9}$$

We found here sufficient to set the exponents $p = 0.6$ and $q = 1.1$ to the values obtained by fitting the kink-pair formation enthalpy in pure iron with Proville potential and to only adjust ΔH_0 and τ_P. The fits are shown as continuous lines in Figs. 10(c) and 10(d), while the values of $\Delta H_{0,i}(L)$ and $\tau_{P,i}(L)$ are reported in Figs. 10(e) and 10(f). They represent the effect of the solute spacing on the activation enthalpy. We found $\Delta H_{0,1} \approx \Delta H_{0,2}$, independent of L and only slightly larger than the value in pure iron [see Fig. 10(e)]. For the sake of simplicity, we used their average value, ΔH_0, in the model. The effective Peierls stresses $\tau_{P,i}$ on the other hand strongly depend on the solute spacing and are different for the first and second barrier. As seen in Fig. 10(f), they can be accurately fitted as

$$\tau_{P,i}(L) = \frac{a_i}{(L/b)^{b_i}} + c_i \tag{10}$$

with $a_1 = 7.89\times10^5\,\mathrm{MPa}$, $b_1 = 3.0$, $c_1 = 959\,\mathrm{MPa}$, $a_2 = 7.10\times10^5\,\mathrm{MPa}$, $b_2 = 2.7$, and $c_2 = 1.01\times10^3\,\mathrm{MPa}$. The strong dependence of ΔH_2 on L seen in Figs. 10(c) and 10(d) implies that short segments have a much reduced nucleation probability compared to larger segments, resulting in the negligible effect of ℓ observed in Sec. V B.

The unpinning stresses obtained from Eq. (6) with the continuous approximation of ΔH_i in Eq. (9) and the attempt frequency and activation entropy computed in pure iron are shown as a dashed line in Fig. 9. The model reproduces the strong pinning effect at short solute spacing, which is caused

by the increased activation enthalpy, and the convergence to the flow stress in pure iron at large spacing. In between, the model tends to underestimate the pinning stress.

However, we have made a strong simplification by assuming that the activation entropy ΔS was not affected by the solute atoms. We can reasonably expect that the presence of solute atoms along the dislocation will affect the vibrational modes of the system and thus modify the activation entropy. We attempted to perform free energy barrier calculations with the PAFI method in the case of Fe-C but faced difficulties as carbon tends to migrate to neighboring sites during the sampling at finite temperature. Short segments of a few Burgers vectors are not long enough to support kink pairs, and the line advances while remaining straight. We expect in this case a much reduced activation entropy compared to the kink pair mechanism, since the vibration modes of two straight segments are less different than a straight line and a dislocation with a kink pair. For longer segments on the other hand, the usual kink-pair mechanism remains applicable, and the behavior of pure Fe should be recovered, i.e., $\Delta S = \alpha_{\mathrm{Fe}} k_B \tau$. In order to assess the possible effect of a length-varying activation entropy which increases with L and smoothly tends to the value of pure iron, we tested a simple phenomenological law $\alpha(L) = \alpha_{\mathrm{Fe}} \tanh(\frac{L}{100b})$ for both barriers. This is again a simplification since we can expect the activation entropy to vary differently for both barriers.

Adding this length dependence of the entropy to Eqs. (9) and (6), we obtain a model shown as a continuous line in Fig. 9, with a greatly improved agreement with MD simulations, thanks to the simple phenomenological law. This suggests that the activation entropy is reduced for closely spaced defects. This interesting investigation is left for future work.

VI. CONCLUSION AND PERSPECTIVES

We used atomistic simulations to study the interaction of screw dislocations with interstitial carbon atoms in iron. Simulations of full solid solutions showed a strong locking caused by the short-range attraction between the dislocation and the solutes. The contributions of all carbon atoms close to the dislocation line result in a collective effect that amplifies the strengthening.

In order to clarify the origin of this strengthening and to overpass the difficulty to analyze such collective effect in MD simulations, we focused on elementary interaction processes between a screw dislocation and an array of carbon atoms. Though generally neglected, the effect of entropy was found significant when comparing the predictions of the model to the MD simulations. We incorporated a stress- and length-dependent activation entropy using a phenomenological approach. A more detailed study, based on free energy calculations in the FeC system for different solute spacings and levels of stress, would be very valuable and is an important perspective of this work.

We have shown here that the elementary interaction process between a screw dislocation and carbon atoms involves the successive nucleation of two kink pairs since a carbon atom can block a single kink and prevent its annihilation with a kink on the other side at least on MD timescale. We can expect this short-range effect to be general to alloys with strong short-range attractive interactions, where solutes have a finite capture radius for dislocations. This applies to many bcc solid solutions with interstitial solutes [15,23]. In that regard, since DFT calculations predict a larger capture radius than the present potential, we can expect that more than two kinks may be needed to unpin a dislocation in a *real* FeC alloy, leading to an even stronger pinning effect as reported here. These elementary processes could be implemented in a kinetic Monte Carlo model of dislocation pinning as developed in Refs. [71,78,79]. Such a model would allow the study of the complex and collective interplay between solute-dislocation interactions and stress-mediated solute diffusion leading to the formation of Cottrell atmospheres, over length and timescales unaccessible to MD simulations.

ACKNOWLEDGMENT

We gratefully acknowledge support from the CNRS/IN2P3 Computing Center (Lyon — France) for providing computing and data-processing resources needed for this work.

[1] H. Berns and W. Theisen, *Ferrous Materials: Steel and Cast Iron* (Springer, Berlin, Heidelberg, 2008), pp. 1–418.
[2] D. Bacon, Y. Osetsky, and D. Rodney, *Dislocations in Solids*, edited by J. P. Hirth and L. Kubin (Elsevier, 2009), pp. 1–90.
[3] D. Caillard and J.-L. Martin, *Thermally Activated Mechanisms in Crystal Plasticity* (Elsevier, Amsterdam, 2003).
[4] L. Proville and D. Rodney, Modeling the thermally activated mobility of dislocations at the atomic scale, in *Handbook of Materials Modeling: Methods: Theory and Modeling*, edited by W. Andreoni and S. Yip (Springer International Publishing, Cham, 2020), pp. 1525–1544.
[5] D. Caillard, Acta Mater. **59**, 4974 (2011).
[6] S. Patinet and L. Proville, Phys. Rev. B **78**, 104109 (2008).
[7] F. Maresca and W. A. Curtin, Acta Mater. **182**, 144 (2020).
[8] S. I. Rao, C. Woodward, B. Akdim, O. N. Senkov, and D. Miracle, Acta Mater. **209**, 116758 (2021).
[9] C. R. LaRosa, M. Shih, C. Varvenne, and M. Ghazisaeidi, Mater. Charact. **151**, 310 (2019).
[10] C. Varvenne, G. Leyson, M. Ghazisaeidi, and W. Curtin, Acta Mater. **124**, 660 (2017).
[11] A. Ghafarollahi, F. Maresca, and W. Curtin, Modell. Simul. Mater. Sci. Eng. **27**, 085011 (2019).
[12] R. Labusch, Physica Status Solidi (B) **41**, 659 (1970).
[13] T. Suzuki, S. Takeuchi, and H. Yoshinaga, *Dislocation Dynamics and Plasticity*, Springer Series in Materials Science Vol. 12 (Springer, Berlin, Heidelberg, 1991).
[14] L. Ventelon, B. Lüthi, E. Clouet, L. Proville, B. Legrand, D. Rodney, and F. Willaime, Phys. Rev. B **91**, 220102(R) (2015).
[15] B. Lüthi, L. Ventelon, D. Rodney, and F. Willaime, Comput. Mater. Sci. **148**, 21 (2018).
[16] D. Rodney, L. Ventelon, E. Clouet, L. Pizzagalli, and F. Willaime, Acta Mater. **124**, 633 (2017).

[17] C. Woodward and S. I. Rao, Phys. Rev. Lett. **88**, 216402 (2002).

[18] M. Itakura, H. Kaburaki, and M. Yamaguchi, Acta Mater. **60**, 3698 (2012).

[19] L. Ventelon, F. Willaime, E. Clouet, and D. Rodney, Acta Mater. **61**, 3973 (2013).

[20] L. Dezerald, L. Ventelon, E. Clouet, C. Denoual, D. Rodney, and F. Willaime, Phys. Rev. B **89**, 024104 (2014).

[21] L. Dezerald, D. Rodney, E. Clouet, L. Ventelon, and F. Willaime, Nat. Commun. **7**, 11695 (2016).

[22] A. Kraych, E. Clouet, L. Dezerald, L. Ventelon, F. Willaime, and D. Rodney, npj Comput. Mater. **5**, 109 (2019).

[23] B. Lüthi, L. Ventelon, C. Elsässer, D. Rodney, and F. Willaime, Modell. Simul. Mater. Sci. Eng. **25**, 084001 (2017).

[24] B. Lüthi, Modélisation ab initio des interactions dislocation-soluté dans les métaux de transition cubiques centrés, Ph.D. thesis, Université de Lyon, 2017.

[25] G. Hachet, L. Ventelon, F. Willaime, and E. Clouet, Acta Mater. **200**, 481 (2020).

[26] J. Chaussidon, M. Fivel, and D. Rodney, Acta Mater. **54**, 3407 (2006).

[27] J. Marian, W. Cai, and V. V. Bulatov, Nat. Mater. **3**, 158 (2004).

[28] K. Tapasa, A. V. Barashev, D. J. Bacon, and Y. N. Osetsky, J. Nucl. Mater. **361**, 52 (2007).

[29] R. G. Veiga, M. Perez, C. S. Becquart, E. Clouet, and C. Domain, Acta Mater. **59**, 6963 (2011).

[30] O. Waseda, R. G. Veiga, J. Morthomas, P. Chantrenne, C. S. Becquart, F. Ribeiro, A. Jelea, H. Goldenstein, and M. Perez, Scr. Mater. **129**, 16 (2017).

[31] S. M. Zamzamian, S. A. Hossein Feghhi, and M. Samadfam, J. Nucl. Mater. **527**, 151806 (2019).

[32] A. Ishii, J. Li, and S. Ogata, PLoS ONE **8**, e60586 (2013).

[33] R. G. Veiga, H. Goldenstein, M. Perez, and C. S. Becquart, Scr. Mater. **108**, 19 (2015).

[34] C. S. Becquart, J. Raulot, G. Bencteux, C. Domain, M. Perez, S. Garruchet, and H. Nguyen, Comput. Mater. Sci. **40**, 119 (2007).

[35] E. Clouet, S. Garruchet, H. Nguyen, M. Perez, and C. S. Becquart, Acta Mater. **56**, 3450 (2008).

[36] Y. Hanlumyuang, P. A. Gordon, T. Neeraj, and D. C. Chrzan, Acta Mater. **58**, 5481 (2010).

[37] Y. Wang, X. Wang, Q. Li, B. Xu, and W. Liu, J. Mater. Sci. **54**, 10728 (2019).

[38] V. Bulatov, V. V. Bulatov, and W. Cai, *Computer Simulations of Dislocations* (Oxford University Press on Demand, 2006), Vol. 3.

[39] F. Maresca, D. Dragoni, G. Csányi, N. Marzari, and W. A. Curtin, npj Comput. Mater. **4**, 69 (2018).

[40] D. Dragoni, T. D. Daff, G. Csányi, and N. Marzari, Phys. Rev. Materials **2**, 013808 (2018).

[41] H. Mori and T. Ozaki, Phys. Rev. Materials **4**, 040601(R) (2020).

[42] S. Starikov, D. Smirnova, T. Pradhan, Y. Lysogorskiy, H. Chapman, M. Mrovec, and R. Drautz, Phys. Rev. Materials **5**, 063607 (2021).

[43] R. Alexander, L. Proville, C. S. Becquart, A. M. Goryeava, J. Dérès, C. Lapointe, and M.-C. Marinica, J. Nucl. Mater. **535**, 152141 (2020).

[44] S. Plimpton, J. Comput. Phys. **117**, 1 (1995).

[45] P. A. Gordon, T. Neeraj, Y. Li, and J. Li, Modell. Simul. Mater. Sci. Eng. **18**, 085008 (2010).

[46] T. Lee, M. I. Baskes, S. M. Valone, and J. D. Doll, J. Phys.: Condens. Matter **24**, 225404 (2012).

[47] B.-J. Lee, M. I. Baskes, H. Kim, and Y. K. Cho, Phys. Rev. B **64**, 184102 (2001).

[48] M. Müller, P. Erhart, and K. Albe, J. Phys.: Condens. Matter **19**, 326220 (2007).

[49] D. J. Hepburn and G. J. Ackland, Phys. Rev. B **78**, 165115 (2008).

[50] R. G. Veiga, C. S. Becquart, and M. Perez, Comput. Mater. Sci. **82**, 118 (2014).

[51] B.-J. Lee, Acta Mater. **54**, 701 (2006).

[52] K. O. E. Henriksson and K. Nordlund, Phys. Rev. B **79**, 144107 (2009).

[53] L. S. I. Liyanage, S.-G. Kim, J. Houze, S. Kim, M. A. Tschopp, M. I. Baskes, and M. F. Horstemeyer, Phys. Rev. B **89**, 094102 (2014).

[54] L. Proville, D. Rodney, and M. C. Marinica, Nat. Mater. **11**, 845 (2012).

[55] G. Ackland, M. Mendelev, D. Srolovitz, S. Han, and A. Barashev, J. Phys.: Condens. Matter **16**, S2629 (2004).

[56] E. Clouet, L. Ventelon, and F. Willaime, Phys. Rev. Lett. **102**, 055502 (2009).

[57] D. Rodney, Acta Mater. **52**, 607 (2004).

[58] D. Rodney, Phys. Rev. B **76**, 144108 (2007).

[59] W. M. Brown, P. Wang, S. J. Plimpton, and A. N. Tharrington, Comput. Phys. Commun. **182**, 898 (2011).

[60] A. Stukowski, Modell. Simul. Mater. Sci. Eng. **18**, 015012 (2009).

[61] G. Henkelman, B. P. Uberuaga, and H. Jónsson, J. Chem. Phys. **113**, 9901 (2000).

[62] G. T. Barkema and N. Mousseau, Phys. Rev. Lett. **77**, 4358 (1996).

[63] R. Malek and N. Mousseau, Phys. Rev. E **62**, 7723 (2000).

[64] See Supplemental Material at http://link.aps.org/supplemental/10.1103/PhysRevMaterials.6.013608 for details on the availability, development, and alloy properties of the hybrid interatomic potential, which includes Refs. [80,81].

[65] L. Ventelon and F. Willaime, J. Comput.-Aided Mater. Des. **14**, 85 (2007).

[66] L. Kubin, *Oxford Series on Materials Modelling* (Taylor & Francis, 2013).

[67] M. I. Mendelev, S. Han, D. J. Srolovitz, G. J. Ackland, D. Y. Sun, and M. Asta, Philos. Mag. **83**, 3977 (2003).

[68] L. Proville, L. Ventelon, and D. Rodney, Phys. Rev. B **87**, 144106 (2013).

[69] D. Brunner and J. Diehl, Physica Status Solidi (a) **124**, 455 (1991).

[70] S. Narayanan, D. L. McDowell, and T. Zhu, J. Mech. Phys. Solids **65**, 54 (2014).

[71] S. Shinzato, M. Wakeda, and S. Ogata, Int. J. Plast. **122**, 319 (2019).

[72] A. M. Goryaeva, J. Dérès, C. Lapointe, P. Grigorev, T. D. Swinburne, J. R. Kermode, L. Ventelon, J. Baima, and M.-C. Marinica, Phys. Rev. Materials **5**, 103803 (2021).

[73] D. S. Tchitchekova, J. Morthomas, F. Ribeiro, R. Ducher, and M. Perez, J. Chem. Phys. **141**, 034118 (2014).

[74] A. Stukowski, V. V. Bulatov, and A. Arsenlis, Modell. Simul. Mater. Sci. Eng. **20**, 085007 (2012).

[75] C. L. Kelchner, S. J. Plimpton, and J. C. Hamilton, Phys. Rev. B **58**, 11085 (1998).

[76] T. D. Swinburne and M.-C. Marinica, Phys. Rev. Lett. **120**, 135503 (2018).

[77] A. Allera, T. D. Swinburne, C.-M. Marinica, M. Perez, F. Ribeiro, and D. Rodney (unpublished).

[78] Y. Zhao and J. Marian, Modell. Simul. Mater. Sci. Eng. **26**, 045002 (2018).

[79] Y. Zhao, L. Dezerald, M. Pozuelo, X. Zhou, and J. Marian, Nat. Commun. **11**, 1227 (2020).

[80] G. J. Ackland and G. Bonny, in *Comprehensive Nuclear Materials*, edited by R. J. Konings and R. E. Stoller, 2nd ed. (Elsevier, Oxford, 2020), pp. 544–572.

[81] H. Schultz, Mater. Sci. Eng. **3**, 189 (1968).